

pubs.acs.org/cm Article

Size Dependent Optical Properties and Structure of ZnS Nanocrystals Prepared from a Library of Thioureas

Ellie Bennett, Matthew W. Greenberg, Abraham J. Jordan, Leslie S. Hamachi, Soham Banerjee, Simon J. L. Billinge, and Jonathan S. Owen*



Cite This: Chem. Mater. 2022, 34, 706-717



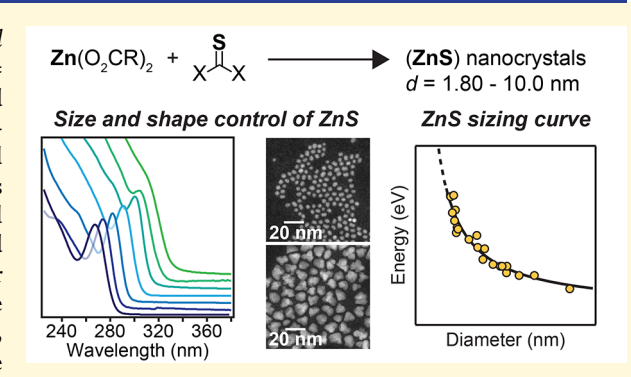
ACCESS

III Metrics & More

Article Recommendations

s Supporting Information

ABSTRACT: ZnS nanocrystals $(\lambda_{\rm max}(1S_{\rm e}-1S_{\rm 3/2h})=260-320$ nm, d=1.7-10.0 nm) are synthesized from Zn(O₂CR)₂ (O₂CR = tetradecanoate, oleate and 2-hexyldecanoate), N_iN' -disubstituted and $N_iN'_iN'$ -trisubstituted thioureas, and P_iP_iN -trisubstituted phosphanecarbothioamides. The influence of precursor substitution, ligand sterics, and reaction temperature on the final nanocrystal size was evaluated. Using saturated hydrocarbon solvents and saturated aliphatic carboxylate ligands, polymeric byproducts could be avoided and pure ZnS nanocrystals isolated. Elevated temperatures, slower precursor conversion reactivity, and branched zinc 2-hexyldecanoate yield the largest ZnS nanocrystals. Carefully purified zinc carboxylate, rapidly converting precursors, and cooling the synthesis mixture following complete precursor conversion provide quasispherical



nanocrystals with the narrowest shape dispersity. Nanocrystal sizes were measured using pair distribution function (PDF) analysis of X-ray scattering and scanning transmission electron microscopy (STEM) and plotted versus the energy of their first excitonic optical absorption. The resulting empirical relationship provides a useful method to characterize the nanocrystal size from 1.7 to 4.0 nm using optical absorption spectroscopy.

■ INTRODUCTION

Semiconductor nanocrystals that emit visible light, including CdS, CdSe, CdSe/CdS, ZnSe, and InP, are highly desirable for solid-state lighting, imaging, electroluminescent displays, and down conversion applications. 1-3 ZnS plays an important role in many of these technologies as a shell material that improves the optical performance of emissive cores. Its wide band gap (zinc blende (ZB): 3.74 eV, wurtzite (WZ): 3.77 eV)⁴ provides a barrier layer that passivates surface traps and confines the exciton to the core, increasing the photoluminescence quantum yield (PLQY).^{5,6} ZnS is also a common host for luminescent dopants (e.g., Co²⁺, Cu²⁺, Pb²⁺, and Mn²⁺, mono- or dual-doped) with long-lived excited lifetimes, useful for sensing and imaging applications.⁷⁻¹⁰ Furthermore, pure ZnS nanocrystals can serve as a seed for more complex heterostructures such as blue-emitting spherical quantum wells (i.e., ZnS/ZnSeTe/ZnS), 11 whose architecture mitigates interfacial strain and further increases PLQY.12

Unsurprisingly, a variety of methods have been developed to grow ZnS shells. To control the reactivity and ensure shells grow without separately nucleating ZnS, precursors are often added slowly via a syringe pump, $^{13-15}$ in sequential steps, such as in successive ion layer adsorption and reaction (SILAR), $^{16-20}$ or colloidal atomic layer deposition (c-ALD) methods. 21,22 However, the synthesis of colloidal ZnS

nanocrystals is less well developed, especially when compared to colloidal CdE nanocrystals (E = S, Se, Te). 23,24 While a variety of syntheses have been reported, including examples in aqueous media, $^{25-32}$ those that use elemental sulfur or thioacetamide precursors, $^{33-41}$ or single-source precursors, 42,43 it remains challenging to finely control ZnS nanocrystal sizes. Many examples achieve sizes too large to exhibit quantum confinement or require the precursor reaction to be terminated prematurely to obtain small sizes. 33,36,43,44 Other reports describe problems with colloidal stability and aggregation. $^{30,37,45-47}$

Similarly, controlling the shape of ZnS is very important to optoelectronic properties and spectral line widths. While ZnS nanoplatelets, ^{48–50} nanorods, ^{49,51} and nanowires ^{48,52} have all been reported, the characterization and uniformity of these shapes lags behind heavier II–VI counterparts. In addition, ZnS shells often form islands that are attributed to the effects of interfacial strain. ^{53,54} Improved synthetic methods that

Received: October 4, 2021 Revised: December 13, 2021 Published: January 6, 2022





control these structural features could improve the performance of emissive quantum dots.

These synthetic issues are further compounded by the challenge of accurately monitoring and characterizing the products. Ultraviolet (UV) absorption spectroscopy measurements are complicated by the absorbance of solvents, precursors, and coproducts. While extinction coefficients for the related cadmium and lead chalcogenides are known, 55–58 no such measurements on ZnS have been reported, preventing particle concentrations and yields from being easily extracted from UV absorbance spectra.

There is also significant disagreement between reports describing the size dependence of the absorption spectrum of ZnS. 28,42,59 The inconsistencies are likely the result of error in common sizing methods, including electron microscopy (EM), leading to a range in nanocrystal sizes reported for the same energy of transition (Figure S32 and Tables S3-S5). 27-33,37,40-43,47,59-66 Compared to CdE and PbE materials, ZnS has a lower Z-contrast, making EM techniques challenging, especially for the smallest nanocrystals. Scherrer analysis of powder X-ray diffraction (pXRD) is also limited at very small sizes, especially when stacking faults and inhomogeneous strain contribute to peak broadening.6 Mass spectrometry has been used to probe ZnS QD ensembles; 68,69 however, zinc isotope patterns, broad distributions that depend on ligands and their coverage, as well as the formation of multiply charged species and fragmentation complicate the interpretation of this data. The sizes of nanocrystals have also been estimated using the Brus equation, 70,71 which is known to overestimate sizes, particularly for ZnS nanocrystals $(d < 3 \text{ nm})^{2}$

X-ray scattering techniques such as small-angle X-ray scattering (SAXS) and X-ray pair distribution function (PDF) analysis are valuable tools for probing nanocrystal structures. Recently, SAXS has been used to confirm the sizing curves for several metal chalcogenide nanocrystals. PDF analysis is especially useful due to its sub-Ångstrom level resolution. This has enabled the determination of crystallite sizes and characterization of crystal structures, and internal stacking faults have been demonstrated in different nanocrystal systems, 74,77,78 including ZnS. 79,80

Following previous work on the synthesis of PbS and CdS nanocrystals from thiourea derivatives, ^{81,82} we targeted a synthesis of ZnS nanocrystals that would provide narrow size distributions and ready access to a range of sizes. With such nanocrystals in hand, we report a comparison between the optical spectrum and the size as measured with high-angle annular dark-field scanning transmission electron microscopy (HAADF-STEM, referred to herein as STEM) and PDF analysis. The effect of precursor structure, surfactants, and temperature on the final crystal size and shape is described.

■ RESULTS AND DISCUSSION

ZnS nanocrystals were synthesized by the reaction of $Zn(O_2CR)_2$ (O_2CR = tetradecanoate, oleate, and 2-hexyldecanoate) with N,N'-disubstituted and N,N',N'-trisubstituted thioureas, and a novel class of metal sulfide precursors: P,P-phenyl, N-substituted phosphanecarbothioamides (1–3, Table 1). The sulfur precursors were dissolved in tetraglyme (5% of total reaction volume) and injected into the preheated zinc carboxylate solution. Syntheses were conducted under an inert atmosphere over a wide range of temperatures (130–280 °C), sulfur precursor concentrations (5–100 mM), and Zn/S ratios

Table 1. Substituted Phosphanecarbothioamide and Thiourea Precursors Used in This Study

	X_1	X_2
1a	$NH(n-C_6H_{13})$	$NH(n-C_{12}H_{25})$
1b	NH(4-CF ₃ -Ph)	$NH(n-C_{12}H_{25})$
1c	NH(i-Pr)	NH(i-Pr)
1d	NH(Ph)	NH(Ph)
2a	NH(n-Bu)	$N(n-Bu)_2$
2b	NH(Ph)	$N(n-Bu)_2$
2c	NH(Ph)	N(CH ₃)Ph
2d	$NH(n-C_6H_{13})$	$N(n-C_8H_{17})_2$
2e	$NH(n-C_{12}H_{25})$	pyrrolidine
2f	NH(4-MeO-Ph)	$N(n-Bu)_2$
2g	NH(4-CF ₃ -Ph)	$N(n-Bu)_2$
3a	NH(Ph)	PPh_2
3b	$NH(4-CF_3-Ph)$	PPh_2

(1.5-3.0:1) (Scheme 1 and Figure S1). Tuning the precursor substitution pattern, carboxylate structure, and reaction

Scheme 1. Standard Reaction Conditions for the Synthesis of ZnS Nanocrystals from Zinc Carboxylates and a Substituted Thiourea Listed in Table 1

$$1.5 \, {\rm Zn}({\rm O_2CR})_2 + \begin{array}{c} {\rm S} \\ {\rm X} \\ \end{array} \\ {\rm X} \\ \end{array} \\ \begin{array}{c} {\rm 130 - 280 \ ^oC, \ 20 \ mM} \\ {\rm 95\% \ hexadecane} \\ {\rm or \ 1-octadecene} \\ {\rm 5\% \ tetraglyme} \\ \\ {\rm X = NR_{2^1} \ PR_2} \\ {\rm O_2CR_2 = \ oleate, \ tetradecanoate, } \\ {\rm 2-hexyl \ decanoate} \\ \end{array} \\ \begin{array}{c} {\rm d = 1.7 - 10.0 \ nm} \\ {\rm \lambda}(1S_{\rm o} - 1S_{\rm 1/2h}) = 260 - 320 \ nm \\ \end{array}$$

temperature allowed a range of sizes (d=1.7-10.0~nm) to be synthesized whose lowest energy excitonic transitions ($\lambda_{\text{max}}(1\text{S}_{\text{e}}-1\text{S}_{3/2\text{h}})$) span 260–320 nm (Figure 1).

STEM analysis confirms that the resulting nanocrystals have small size polydispersity (percent dispersity, $\sigma/d=7-16\%$) and morphology that varied from quasispherical to more irregular shapes depending on the reaction conditions (see detailed discussion below). The size of quasispherical nanocrystals is compared to the corresponding excitonic absorption energy to generate an empirical sizing formula. The formula was used to estimate the size of nanocrystals from the UV absorption spectra of reaction aliquots in the following sections.

When synthesized in 1-octadecene (ODE), the ZnS nanocrystal product is not easily separated from polymeric coproducts, ⁸³ as was observed using ¹H nuclear magnetic resonance (NMR) spectroscopy (Figures S2 and S3). Postsynthetic exchange of oleate ligands with 6-[2-[2-(2-methoxyethoxy)-ethoxy]-ethoxy]hexyl phosphonate (Figure S4) allows removal of polymerized ODE, if necessary. ⁸³ In contrast to other nanocrystal syntheses, ^{84,85} thiourea conversion does not rely on the reactivity of an unsaturated solvent, so it can be replaced with a saturated hydrocarbon to eliminate polymeric coproducts. At reaction temperatures below 280 °C, *n*-hexadecane (bp = 287 °C) can be used, while squalane (bp = 350 °C) can be used at higher temperatures.

Zinc oleate decomposes to ZnO (band gap = 3.37 eV) when heated at elevated temperatures (>310 °C) and in the presence of oleic acid and/or oleylamine. Ref. We therefore avoid these surfactant additives and use the thiourea library to identify precursors that convert appropriately at lower temperatures

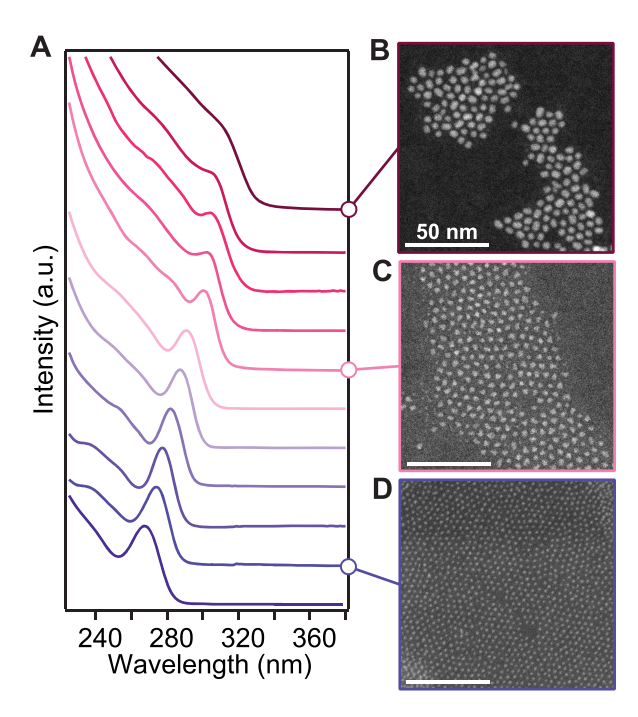


Figure 1. (A) UV absorption spectra of isolated ZnS nanocrystals used to create the sizing curve. (B–D) HAADF-STEM images for corresponding UV absorption spectra showcase the range of sizes that can be obtained (scale bars = 50 nm). Synthetic parameters for all sizing samples are included in the Supporting Information (Table S6).

(<280 °C). Nonetheless, the stability of zinc carboxylate precursors was probed. While the solutions of zinc oleate in octadecene remain clear and colorless, with no significant change in the UV—vis absorption spectra below 260 °C, turbid yellow mixtures form in hexadecane in less than an hour (Figure S5). The solutions of zinc tetradecanoate in hexadecane, on the other hand, remain clear and colorless after 2 h at 260 °C. These experiments demonstrate that zinc carboxylates can be used to synthesize ZnS in alkane solvents without significant problems with decomposition. ZnS produced from the two sets of the solvent and metal carboxylates have similar final $\lambda_{\rm max}$ values.

Factors Influencing Nanocrystal Size. The final nanocrystal diameter can be tuned by adjusting the precursor conversion reactivity, the carboxylate structure, and the synthesis temperature. It is well established that the precursor conversion kinetics can be used to control the extent of nucleation and the final size following complete precursor conversion. ^{81,82,88–90} By modifying the thiourea structure, the conversion reactivity can be finely adjusted across a wide range of temperatures. Decreasing precursor reactivity produces larger nanocrystals (Figures 2 and S8). The reactivity of electron-deficient and sterically unencumbered thioureas with zinc carboxylates is greatest: *N,N'*-disubstituted precursors are most rapid, followed by *N,N',N'*-trisubstituted thioureas and then *P,P*-phenyl, *N*-substituted phosphanecarbothioamides (3a,b, Table 1).

The effect of the thiourea reactivity on the synthesis was monitored using a quantitative, timed aliquoting method and UV absorption spectroscopy. The nanocrystal absorbance, particularly at higher energies in the UV region, can be obscured by precursors, coproducts, and even surfactant ligands and so, on its own, is not a reliable measure of the

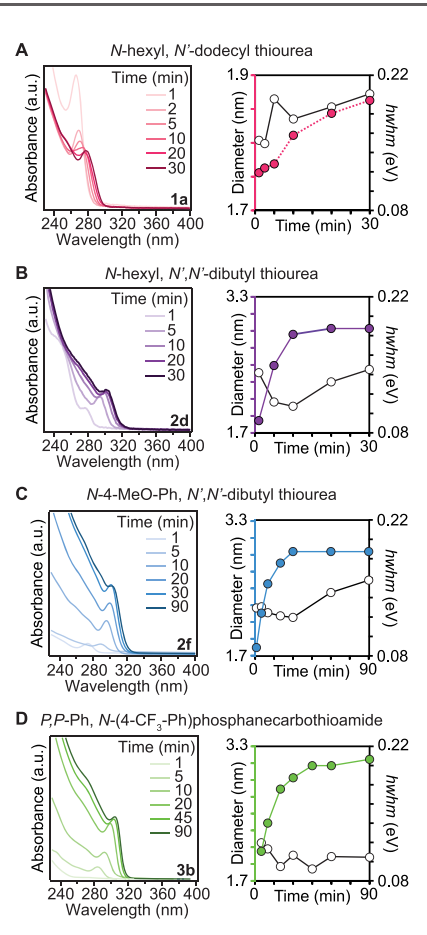


Figure 2. Representative UV—vis absorption spectra of reaction aliquots taken from ZnS syntheses and the diameter and hwhm as a function of reaction time. All reactions are run with zinc oleate unless otherwise noted, at 240 °C, and with the following precursors: (A) 1a, (B) 2d, (C) 2f, and (D) 3b with zinc tetradecanoate.

reaction yield. Instead, the evolution of the size, yield, and polydispersity is monitored by following the position, intensity, and half width at half-maximum (hwhm) of the lowest-energy excitonic feature, in conjunction with the absorbance intensity at higher energies (λ < 240 nm) (Figures 2, S8, and S16).

The evolution of syntheses conducted with N_iN' -disubstituted thioureas are distinct from slower converting $N_iN'_iN'_i$ and $P_iP_iN'_i$ -trisubstituted precursors (Figure 2). At $T \geq 240$ °C, $N_iN'_i$ -disubstituted thioureas undergo rapid conversion, which is followed by slow ripening of nanocrystals. Aliquots from these reactions display a red-shifting and broadening peak (increasing hwhm), without an increase in the absorbance intensity ($\lambda < 240$ nm or λ_{max}) (Figure 2A). At temperatures below 240 °C, a consistent terminal size is formed ($d \sim 1.8$ nm, Figure S9) and, conversely, there is no obvious ripening detected by UV absorption spectroscopy. We hypothesize that at this low temperature, the solutes are entirely consumed by nucleation at early times and any subsequent nanocrystal growth ($T \geq 240$ °C) occurs by a ripening process.

Syntheses conducted with trisubstituted precursors (2 and 3) display a steadily increasing UV absorbance intensity and simultaneous peak red shift, indicative of conventional nanocrystal growth by rate-limiting precursor conversion (Figure 2B–D). Eventually, the absorbance intensity and nanocrystal size plateau, signifying the end of growth driven by precursor conversion, are referred to hereafter as the "reaction"

end point." The hwhm typically reaches a minimum at this point, following which the syntheses should be removed from the heat source to prevent broadening the spectral distribution (Figure 2B–D). Nanocrystals prepared using 3a,b possess narrower first excitonic absorption peaks than similar sizes produced from N,N',N'-trisubstituted precursors. These results are reminiscent of systematic differences in the fwhm between different precursor families documented for CdS.

At longer times, the excitonic feature broadens without an obvious accompanying red shift. STEM analysis of aliquots following the reaction end point confirms no obvious size increases (Figures S22 and S23), except at very long times ($t \sim 6 \times \text{end point}$). The steady final size during this period suggests that the process that broadens the spectrum is not a consequence of Ostwald or aggregative ripening but some other process such as increasing shape polydispersity. Note that, at large sizes ($\lambda_{\text{max}} > 305 \text{ nm}$), weak quantum confinement and greater shape polydispersity (discussed below) make it challenging to ascertain the exact peak position, so UV spectroscopy alone is not able to determine further size increases.

The size at the reaction end point is plotted as a function of the reaction temperature in Figures 3 and S10. When $N_tN'_t,N'_t$

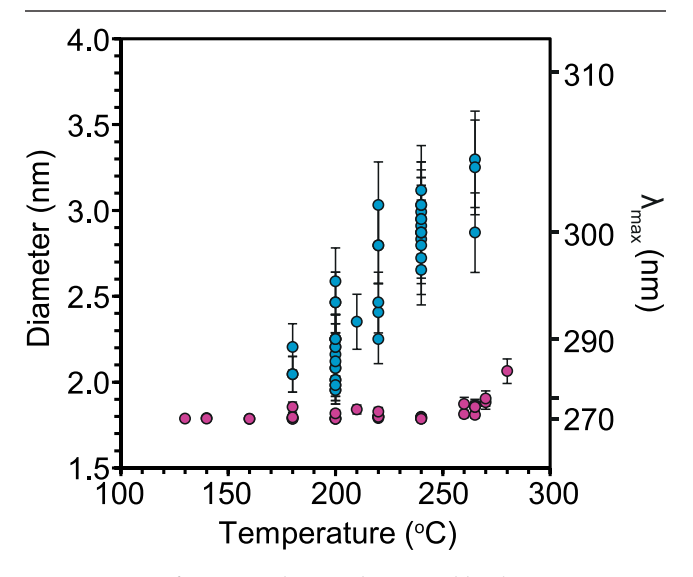


Figure 3. Size of ZnS at end point, determined by the sizing curve, as a function of reaction temperature. ZnS is synthesized from N.N'-disubstituted (pink) and N,N',N'-, P,P,N-trisubstituted (blue) precursors. The plot coded by the specific precursor is shown in the Supporting Information (Figure S10). All reactions use zinc oleate or zinc tetradecanoate and have an initial zinc carboxylate to thiourea precursor ratio of 1.5:1. Error bars are calculated using the uncertainty in the peak energy.

trisubstituted thioureas are used, the final size depends on both the conversion reactivity and the synthesis temperature. Larger sizes are obtained at higher temperatures and when using less reactive thioureas. These results can be explained by a thermally activated growth process that competes with the nucleation process for solutes, as has been reported in PbS, PbSe, and InP systems. ^{91,92}

On the other hand, the size produced by N,N'-disubstituted thioureas is insensitive to the temperature (Figures 3 and S9). The spectra of aliquots consistently display an excitonic feature ($\lambda_{\rm max} \sim 270$ nm, $d \sim 1.75$ nm, ~ 70 ZnS units) that matches a recently reported material proposed to be a magic sized

cluster. Show 240 °C, the final size increases slightly (260–280 °C, $d \sim 1.9$ –2.1 nm), presumably via a ripening mechanism, rather than a precursor conversion limited growth mechanism. At 240 °C, the initial spectra of aliquots red shifts and broadens without increasing in intensity (from d=1.7 to 1.9 nm) (Figure 2B). We interpret these changes to mean that N_iN' -disubstituted thiourea conversion and nucleation are much more rapid than growth beyond $d \sim 1.75$ nm at all temperatures studied here. Above 240 °C, however, ripening mechanisms become important and can lead to larger sizes, while below this temperature, small crystallites are rapidly generated that are stable to ripening. The results described in Figure 3 illustrate the importance of matching the precursor conversion reactivity and the synthesis temperature to gain control over the size.

The influence of the carboxylate chain structure on the size and shape was also investigated. With *N,N'*-disubstituted precursors, optical features and STEM images appear identical regardless of whether oleate or tetradecanoate is used, while the branched zinc 2-hexyldecanoate leads to larger nanocrystals (Figures 4 and S13). For example, switching from oleate to 2-

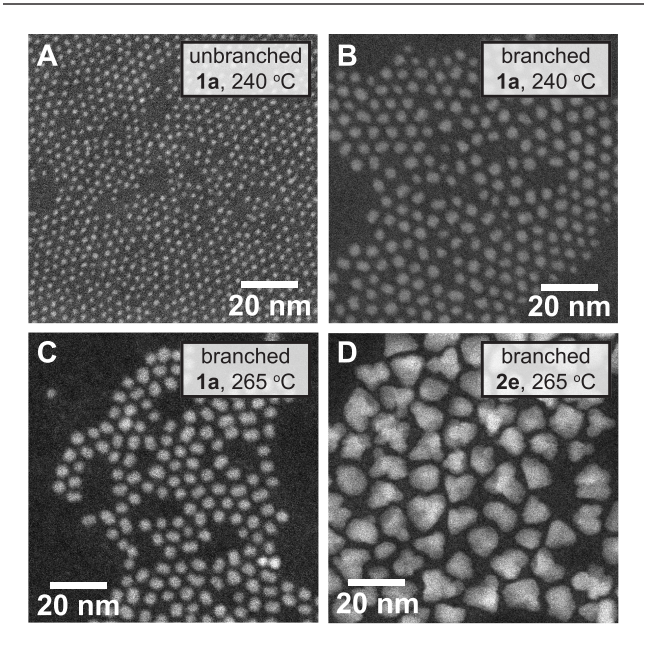


Figure 4. HAADF-STEM images showing replacing unbranched zinc tetradecanoate (A) with branched zinc 2-hexyldecanoate (B–D) results in larger ZnS. The selection of slower thiourea precursors and higher temperature further increases the diameter (D). ZnS sizes: (A) $d=1.9\pm0.2$ nm, percent size polydispersity, $\sigma/d=9.6\%$; (B) $d=3.8\pm0.6$ nm, $\sigma/d=16\%$; (C) $d=4.5\pm0.5$ nm, $\sigma/d=11\%$; and (D) $d=10.1\pm1.3$ nm, $\sigma/d=13\%$.

hexyldecanoate results in nanocrystals with more than twice the diameter (1a, $T=240\,^{\circ}\text{C}$, d=1.9 and 3.8 nm respectively, Figure 4A,B). Larger sizes can also be accessed using higher temperatures and slower precursors. N,N',N'-Trisubstituted thioureas and zinc 2-hexyldecanoate at elevated temperatures ($T=265\,^{\circ}\text{C}$) produce nanocrystals that are too large ($d\sim10\,$ nm) to exhibit quantum confinement. The larger sizes indicate that 2-hexyldecanoate-stabilized nanocrystals grow more rapidly, which may be the result of a reduced ligand coverage.

The final ZnS diameter is most effectively tuned through precursor selection and reaction temperature. Further synthetic

changes, such as adjusting the Zn/S ratio and addition of oleic acid, can also be used to influence the size but increase the size dispersity (Figures S11, S12, S14, and S29). To obtain specific sizes of ZnS, a synthesis guide is provided in the Supporting Information (Tables S1 and S2). Further, synthetic details for all of the samples used in the sizing analysis presented below are provided in Table S6.

Factors Influencing Nanocrystal Shape. ZnS nanocrystals with well-resolved absorption features have an isotropic, quasispherical shape. However, some syntheses produced significant shape polydispersity and broadened optical spectra (Figures S17 and S18). Extensive work to understand the shape polydispersity is described in the Supporting Information (Section II for discussion and Figures S17–S31). Among a variety of factors, the shape polydispersity is sensitive to the chalcogenourea precursor selection, the structure of the carboxylate ligands, the metal precursor purity, and the reaction time. Thus, syntheses can be designed to promote spherical, isotropic growth as described below.

Impure zinc precursors and small impurity ions led to polydisperse products (Figure S18). For example, more irregular shapes were obtained if zinc tetradecanoate was synthesized from zinc nitrate, 95 rather than from zinc trifluoroacetate. The zinc trifluoroacetate preparation allows water to be completely eliminated, and the presence of trifluoroacetate impurities can be ruled out using ¹⁹F NMR spectroscopy (Figure S6).81 Hence, we hypothesize that undetected nitrate, hydroxide, or water impurities in the zinc starting material can induce shape anisotropy. Previous work on other IV-VI and II-VI systems has illustrated the importance of sterically small anions to shape control: cadmium acetate is added to CdSe reactions to form nanoplatelets,⁹⁶ and water impurities in cadmium acetate, thought to lead to hydroxide formation, causes irregularly shaped CdSe nanoplatelets, 97 irregularly shaped PbSe nanocrystals are produced from lead oleate contaminated with lead acetate, 98 and methylphosphonate anions induce II-VI tetrapod formation.⁹⁹ Further, it has recently been reported that nitrate plays a noninnocent role in the synthesis of metal oxide nanocrystals. 100 These observations underscore the importance of pure zinc carboxylate precursors and the advantage of preparing them from metal trifluoroacetates.

Increasingly isotropic shapes are obtained when sterically encumbered chains are used (acetate < tetradecanoate < oleate < 2-hexyldecanoate) (Figures S17, S19, S26, and S27). Adding zinc acetate (10 mol %) to zinc oleate yielded highly anisotropic, tetrapod-like morphologies and broadened optical features (Figure S19). The relationship between ligand bulk and resulting isotropy is not limited to ZnS nanocrystal syntheses. The carboxylate chain bulk also influenced ZnS shell deposition: zinc oleate produced anisotropic shells compared to zinc 2-hexyldecanoate (Figure S21). These observations might be explained by the influence of the chain structure on the extent of surface ligand coverage. Consistent with this hypothesis, it was found that significantly more anisotropic particles were produced when the zinc oleate to thiourea ratio was increased to 3:1, a change that may increase the ligand coverage during growth (Figure S20). We note that this behavior is counter to the influence of metal and chalcogen stoichiometry in the synthesis of PbS. 101,102 Alternatively, these effects may result from the spurious decomposition of zinc carboxylate during the reaction, a process that may depend on the chain structure, as was observed in our study of zinc carboxlyate stability. Together with the purity issues mentioned above, we conclude that the shape anisotropy is caused by the reactivity of the metal precursor.

Faster converting N,N'-disubstituted thioureas also yield more isotropic nanocrystals compared to the slower N,N',N'-trisubstituted precursors. Together with the increased growth kinetics afforded by the branched carboxylate, large, isotropic nanocrystals can be synthesized in short reaction times (Figure 4). We tested whether the effect is the result of the carboxylate structure or the chalcogenourea structure by slowly adding a reactive N,N'-disubstituted thiourea to zinc oleate over the course of 75 min. This approach slows the solute supply kinetics to a rate that matches tri-substituted precursors, and larger, more irregularly shaped nanocrystals are obtained (Figure S30). Thus, anisotropy is not caused by the precursor selection alone and is likely determined by the total reaction time or the rate of growth.

Particular thiourea structures also influenced the shape anisotropy, including the pyrrolidine derivative (2e), which produces tetrapod-like morphologies with featureless UV-absorbance spectra (Figures S22–S24, S26, and S27). On the other hand, even under conditions promoting more anisotropic growth, syntheses employing *P,P*-diphenyl-*N*-substituted phosphanecarbothioamides (3a,b) produce narrow absorbance features (Figure S25). Thus, it appears that the precursor conversion reaction is not orthogonal to the crystal growth in all cases. Similar, albeit smaller, effects were observed in a recent study of CdS.⁸²

Size and Band Gap Relationship. With a range of ZnS sizes in hand (Table S6), we compared the nanocrystal size and the energy of the lowest energy excitonic transition. X-ray PDF and STEM were both used to measure the ZnS nanocrystal sizes (see the Supporting Information, Section III).

All ZnS sizes used to determine the sizing curve were obtained from HAADF-STEM rather than TEM measurements. Size distributions were estimated by measuring several hundred nanocrystals per ZnS sample and fitting the distribution to a Gaussian function (Figure 5, Tables S9-S11, and Appendix I). Twenty-six different ZnS samples yielding spherical or quasispherical nanocrystals were analyzed in this manner. With the exception of five samples, >300 NCs per sample were counted; however, the exclusion of these data points does not impact the extracted sizing curve. Further details and discussion regarding the sizing methods are provided in the Experimental Methods section and Supporting Information, Section III. Percent polydispersities (σ/d , %) of 7-13% in the nanocrystal diameter were found for most samples. This polydispersity corresponds to $\sigma \sim 0.2$ nm in diameter for the smaller sizes, which is approximately the length of a Zn-S bond, further indicating the monodispersity these syntheses achieve. Samples synthesized from zinc 2hexyldecanoate typically had slightly greater size dispersities, despite their greater shape isotropy (Figures S11 and S15).

To help assess STEM results, diameters measured with STEM were compared with crystallite sizes extracted by modeling X-ray PDF data. ZnS nanocrystals were assumed to be spheres, and PDFs were fit using a spherical envelope function and mixed zinc blende and wurtzite ("2-phase") model to extract the nanocrystal diameter, as described previously (Figure 6 and Table S8). Crystallite sizes obtained with the two-phase model are larger and have lower $R_{\rm W}$ values, suggesting the presence of wurtzite stacking faults in a primary zinc blende structure (Figures S33–S38). The sizes extracted

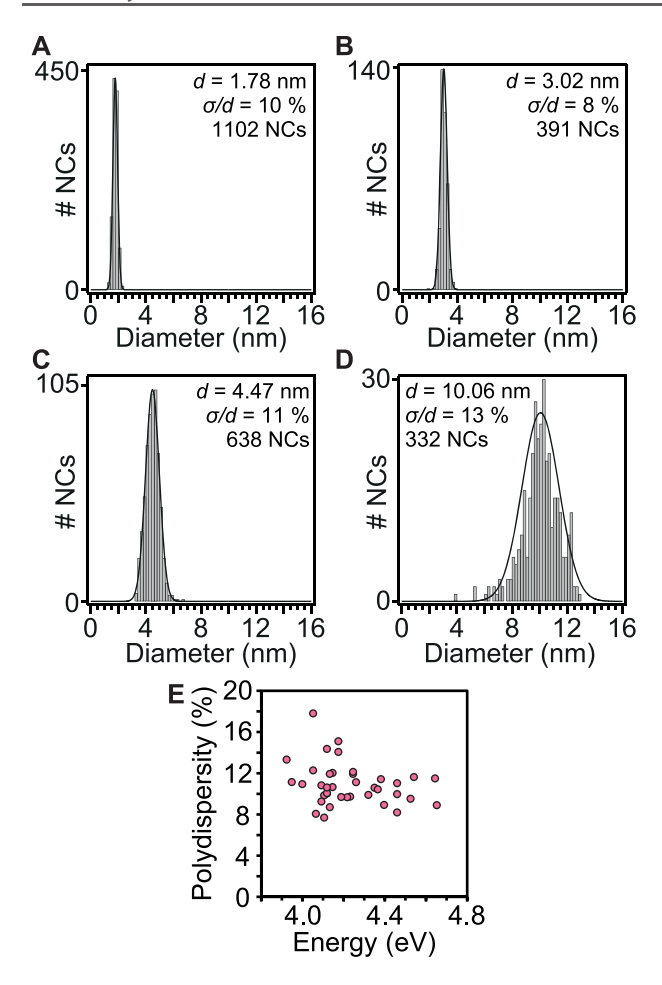


Figure 5. Representative size distributions from STEM analysis of different ZnS sizing samples (A–D). Black lines represent Gaussian curves fit the STEM data. The percent size dispersity $(\sigma/d, \%)$ for the samples ranges from 8 to 16%, with only two samples having a percent dispersity >13%, indicating samples with small polydispersity (E). Sizing samples correspond to Table S6: 8 (A), 7 (B), 17 (C), and 18 (D). Histograms for all samples are included in the Supporting Information (Appendix I).

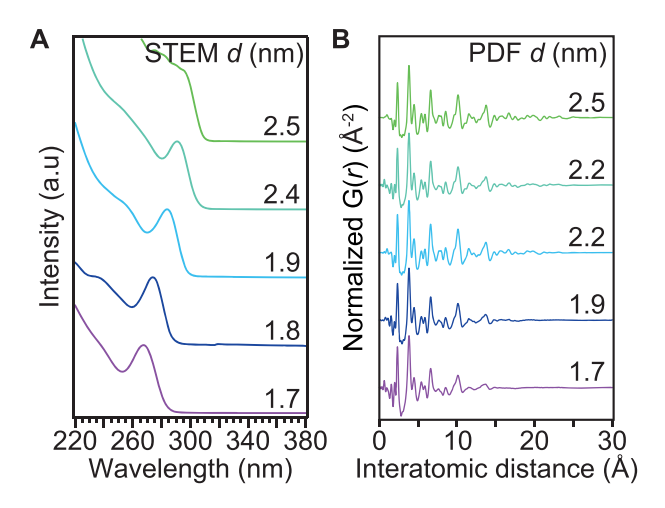


Figure 6. Representative UV absorbance spectra (A) and corresponding PDF data (B). The ZnS diameter is measured by STEM in (A), and PDF data is fit by a two-phase model to extract the crystallite sizes shown in (B).

using the single-phase pure zinc-blende model agree with the trend measured using HAADF-STEM. This confirms the utility of PDF analysis for estimating the diameter of small nanocrystals where EM techniques can struggle. However, PDF modeling underestimates the nanocrystal size above $d \sim 2.1$ nm (Figure S36). Previous PDF studies on ZnS have also shown a discrepancy with TEM for sizing ZnS with d > 2 nm, which was attributed to inhomogeneous strain within the nanocrystal, ⁷⁹ but may also result from multiple crystalline domains within each nanocrystal.

The $E_{\rm 1s-1s}$ is compared to the nanocrystal diameter extracted from STEM in Figure 7 and is fit to eq 1, where $E_{\rm g,bulk}$, a, b, and

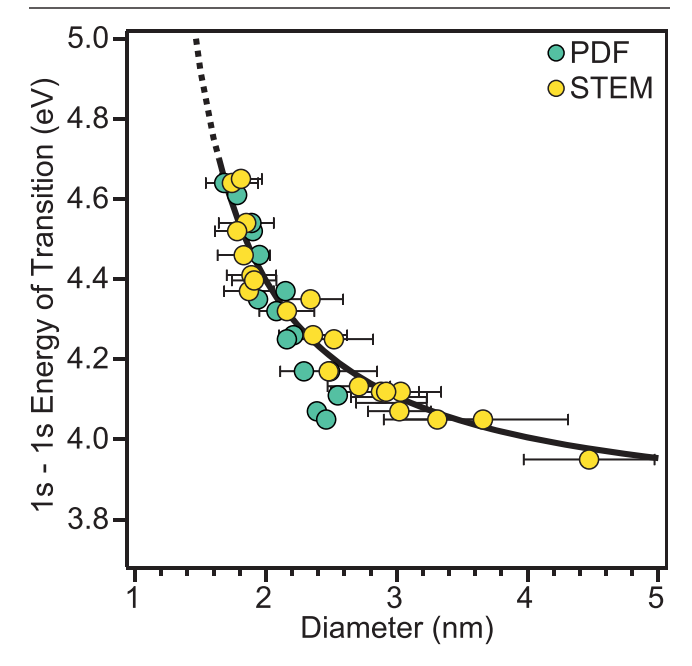


Figure 7. Energy of transition *versus* diameter as determined by STEM (yellow) and PDF (green) analysis. Sizing curve is shown in black. PDF data was not used to create the sizing curve but is shown here for comparison. Error bars represent $d \pm \sigma$, where σ is the standard deviation. Fitting parameters for eq 1: $E_{\rm g,bulk}$ (eV) = 3.801, a (eV⁻¹) = -1.413, b (eV⁻¹ nm⁻¹) = 1.515, c (eV⁻¹ nm⁻²) = 0.01513. For further details, see the Supporting Information, Section III.

c, are fitting parameters summarized in Figure 7. Only quasispherical nanocrystals were used in the analysis. The experimental data spans d=1.7-4.5 nm, and so the fit is valid within this range (3.95–4.64 eV). Additionally, we fit the relationship between wavelength (λ) and diameter (Figure S40). The PDF data was not included in either fit due to the previous discussion but is plotted in Figure 7 for completeness. The $E_{\rm g,bulk}$ value we extract (3.80 eV) lies close to the reported bulk band gap of ZnS (ZB = 3.74 eV, WZ = 3.77 eV)^{27–29,37,42,65,67} despite the fact that strain and crystal phase can alter the band gap.⁴

$$E_{\rm g} = E_{\rm g,bulk} + \frac{1}{a + bd_{\rm NC} + cd_{\rm NC}^2}$$
 (1)

The sizing curve presented in Figure 7 is comparable to other reports at small sizes but deviates for larger nanocrystals (Figure S45). 28,42,59 ZnS has a small exciton Bohr radius (2.5 nm) that makes the size dependence of the band gap relatively weak compared to other metal sulfides. ⁷² Beyond $d \sim 4$ nm excitons in ZnS are only weakly quantum confined, and

increasing the nanocrystal size does not significantly influence the energy of the absorbance spectrum. Thus, the relationship in eq 1 can be used in the range 1.7–4.0 nm ($E_{1s-1s}=3.97-4.64$ eV, $\lambda=266-312$ nm). Further discussion is provided in the Supporting Information, Section III.

CONCLUSIONS

A variety of factors can control the size of ZnS nanocrystals grown in a zinc carboxylate solution, including the thiourea and carboxylate structure and the reaction temperature. Saturated carboxylate surfactants and hydrocarbon solvents increase the stability of the zinc precursor at high temperatures and eliminate polyoctadecene byproducts, improving the product purity. The chain structure and any impurities in zinc precursors influence the size and shape polydispersity, effects that may be related to the total reaction time and the growth kinetics. 2-Hexyldecanoate ligands proved especially valuable for growing large isotropic shapes using more rapid precursors.

By adjusting the conversion reactivity over a wide range, the temperature dependence of the nucleation and growth kinetics can be evaluated. *N*,*N*′-disubstituted thiourea conversion appears to be faster than growth at all temperatures, and thus, the final size is insensitive to thiourea substituents. The conversion of less reactive *N*,*N*′,*N*′-trisubstituted thioureas, however, limits the kinetics of nucleation and growth at all temperatures. Under these conditions, the size depends on temperature and thiourea structure. These results clearly illustrate the importance of controlled reactivity in tailoring the reaction outcome. They also establish an improved relationship between the energy of the first excitonic transition and the nanocrystal size, which will enable the rapid characterization and advancement of ZnS nanocrystal based technologies.

EXPERIMENTAL METHODS

General Methods. All manipulations were performed in air unless otherwise indicated. Acetone, (\geq 99.5%), acetonitrile (\geq 99.5%), aniline (99%), dibutylamine (99.5%), dichloromethane (≥99.5%), diethyl ether (≥99%), dioctylamine (98%), dodecylamine (98%), hexafluorobenzene (99%), hexanes (≥98.5), isopropylamine (≥99.5%), isopropyl isothiocyanate (97%), N-methyl aniline (98%), 4-(methoxy)phenyl isothiocyanate (98%), phenyl isothiocyanate (98%), pyrrolidine(99%), sodium hydroxide (≥98%) triethylamine (≥99%), trifluoroacetic anhydride (≥99%), trifluoroacetic acid (99%), tetradecanoic acid (≥99%), toluene (99.5%), oleic acid (99%), zinc(II) acetate (99.99%), and zinc(II) nitrate (98%) were obtained from Sigma-Aldrich and used without further purification. Pentane and toluene were purchased anhydrous from Sigma-Aldrich and shaken over activated alumina, filtered, and stored over 4 Å molecular sieves in an inert atmosphere glovebox at least 24 h prior to use. Diphenylphosphine (99%) was purchased from Strem and used without further purification. 4-(Trifluoromethyl)phenyl isothiocyanate and dodecyl isothiocyanate were purchased from Santa Cruz Biotechnology and used without further purification. Hexyl isothiocyanate (≥97%), phenyl isocyanate (≥98%), and zinc(II) oxide (99.99%-Zn) were obtained from Alfa Aesar. Butyl isothiocyanate (≥98%) and 2-hexyldecanoic acid (≥98%) were purchased from TCI Chemicals and used without further purification. Hexadecane (99%), 1-octadecene (90%), and tetraethylene glycol dimethyl ether ("tetraglyme," ≥99%) were obtained from Sigma-Aldrich, stirred with calcium hydride overnight, distilled, and stored in a nitrogen glovebox. Benzene-d₆ (99.5%) and chloroform-d (99.8%) were obtained from Cambridge Isotopes and used without further purification. TEM grids were obtained from Ted Pella.

UV—visible absorbance spectra were obtained using a PerkinElmer Lambda 950 spectrophotometer equipped with deuterium and halogen lamps. Transmission electron microscopy (TEM) and scanning transmission electron microscopy (STEM) were performed on a FEI Talos F200X. STEM images were acquired using the high-angle annular dark-field (HAADF) detector with a camera length of 0.205 m, condenser 2 aperture of 50 μ m, and an accelerating voltage of 200 kV. FT-IR spectra were obtained using a PerkinElmer Spectrum 2. Powder X-ray diffraction patterns were measured using a PANalytical X'Pert Powder X-ray diffractometer.

Zinc Oleate Synthesized from Zinc Trifluoroacetate. Zinc oleate is synthesized according to a procedure developed for lead oleate.81 Trifluoroacetic anhydride (4.24 mL, 30 mmol, 1 equiv) and trifluoroacetic acid (0.46 mL, 6 mmol, 0.2 equiv) are added to a mixture of zinc (II) oxide (2.44 g, 30 mmol) and acetonitrile (15 mL) in a 100 mL round-bottom flask. Note: upon addition of trifluoroacetic anhydride or acid, the flask can heat up; an ice bath is kept on hand if temperature rises too far. At room temperature, the white suspension is stirred overnight, resulting in a colorless solution. In a 500 mL Erlenmeyer flask, oleic acid (17.8 g, 63 mmol, 2.1 equiv) and triethylamine (9.83 mL, 71 mmol, 2.35 equiv) are dissolved in 250 mL of dichloromethane at 35 °C. After dissolution, the solution of zinc trifluoroacetate is added dropwise, maintaining the temperature at 35 $^{\circ}$ C. The flask is allowed to cool to room temperature over 1 h and then to -20 °C in a freezer for an additional hour. A white powder is isolated by filtration through a glass fritted filter funnel and washed with acetonitrile (3 \times 200 mL) and diethyl ether (3 \times 200 mL). The white powder is isolated and dried under vacuum for 6 h. Yield is 17.9 g (95%). The purity can be confirmed by ¹H and ¹⁹F NMR. If necessary, further washes can be performed or recrystallization undertaken. The crude product is recrystallized from tetraglyme (~1000 mL); it is dissolved at 120 °C, then cooled to room temperature over 1 h, and then to -20 °C in a freezer for an additional hour. The white powder is isolated and washed as per the earlier step, before being dried under vacuum for 6 h. For additional characterization, see Figures S6 and S7. Note: starting with pure zinc oleate is important for achieving isotropic nanocrystals. The acid to zinc oxide ratio used is higher than the stoichiometric 2:1 to help ensure that there is no remaining unreacted zinc oxide or partially reacted zinc hydroxide, which we suspect also impacts the shape

Zinc Tetradecanoate Synthesized from Zinc Trifluoroacetate. Zinc tetradecanoate is synthesized following the method for zinc oleate, using tetradecanoic acid (14.4 g, 63 mmol, 2.1 equiv) in place of oleic acid. Yield is 15.0 g (96%). For additional characterization, see Figures S6 and S7.

Zinc Tetradecanoate Synthesized from Zinc(II) Nitrate. Zinc tetradecanoate is synthesized according to a procedure developed for cadmium tetradecanoate. Briefly, zinc nitrate (Zn(NO₃)₂·6H₂O, 2.38 g, 8.0 mmol) is dissolved in methanol (40 mL). In a 500 mL Erlenmeyer, tetradecanoic acid (3.84 g, 16.8 mmol) and sodium hydroxide (0.67 g, 16.8 mmol) are dissolved in methanol (200 mL). Upon dissolution, the zinc nitrate solution is added dropwise to the sodium tetradecanoate solution, resulting in the formation of a white precipitate. The flask is cooled to $-20\,^{\circ}\mathrm{C}$ in a freezer for an hour; then, the white precipitate is washed three times with methanol (200 mL) and dried under vacuum for 6 h. Yield = 4.0 g (95%). The product can be recrystallized as described above.

Zinc 2-Hexyldecanoate Synthesized from Zinc Trifluoroacetate. Zinc 2-hexyl decanoate is synthesized following the method for zinc oleate, using 2-hexyl decanoic acid (16.2 g, 63 mmol) in place of the oleic acid. After addition, the flask is stirred for a further 2 h at 40 °C. Then, the flask is cooled to room temperature. Volatiles are removed *in vacuo*, yielding a viscous, colorless oil. The oil is dispersed in toluene (~20 mL) and run through a silica plug three times to purify. Volatiles are removed *in vacuo* and acetone (~20 mL) is added to the crude product. This is gently heated in an Erlenmeyer flask until the product is miscible with the acetone and then cooled to -20 °C in a freezer for 2 h. The acetone is decanted, leaving a colorless oil. This process is repeated twice more before the product is dried under

vacuum for 6 h. Yield is 9.3 g (52%). 1 H NMR (500 MHz, CDCl₃): δ 0.88 (m, 12H), 1.25 (m, 38 H), 1.44 (m, 4H), 1.58 (m, 4H), and 2.33 (m, 2H). 13 C{ 1 H} NMR (125 MHz, CDCl₃): δ 14.23, 14.26, 22.81, 22.84, 27.54, 27.59, 29.42, 29.51, 29.62, 29.78, 31.85, 32.05, and 32.60.

Synthesis of P,P-Phenyl, N-(R)Phosphanecarbothioamides (3a,b). P,P-phenyl and N-(R)phosphanecarbothioamide derivatives are synthesized following a preparation from Itazaki et al. for P,P-phenyl, N-(phenyl)phosphanecarbothioamide. 104

P,P-Phenyl, N-(Phenyl)Phospanecarbothioamide (3a). Briefly, diphenylphosphine (3.79 g, 20.4 mmol) is injected into a Schlenk flask containing phenyl isothiocyanate (2.75 g, 20.4 mmol) and toluene (4 mL) under Ar at room temperature. Upon addition, color change to yellow is observed. The Schlenk flask is heated (~45 °C) for an hour, and the solution turns dark orange. Volatiles are removed in vacuo, yielding a yellow-orange crude solid (6.5 g). The crude product can be recrystallized from ethanol to yield yellow crystals (4.8 g, 73%). 1 H NMR (500 MHz, CDCl₃): δ 7.24 (t, 1H), 7.36 (t, 2H), 7.48 (m, 6H), 7.58 (m, 4 H), 7.64 (d, 2H), and 8.73 (br, 1H). $^{13}\text{C}\{^{1}\text{H}\}$ NMR (125 MHz, CDCl₃): δ 122.48 (d), 127.13, 129.08, 129.44 (d), 130.44, 134.50 (d), 134.70 (d), 138.90, and 206.86 (d). $^{31}P\{^{1}H\}$ NMR (202 MHz, CDCl₃): δ 19.35. Anal. calcd for C₁₉H₁₆NPS: C, 71.01; H, 5.02; N, 4.36. Found: C, 70.82; H, 5.40; and N, 4.35. MS (ASAP) m/z calcd for $[C_{19}H_{16}NPS + H^+]$: 322.08. Found: 322.08.

P,P-Phenyl, N-(4-CF₃-Phenyl)Phospanecarbothioamide (*3b*). This is synthesized as outlined for *P,P*-phenyl, *N*-(phenyl)-phosphanecarbothioamide, with the following adaption: 4-CF₃-phenyl isothiocyanate is used in place of phenyl isothiocyanate. The crude yellow product is recrystallized from ethanol to yield yellow crystals of 3b (2.0 g, 66%). 1 H NMR (500 MHz, CDCl₃): δ 7.48 (m, 6H), 7.58 (m, 6H), 7.80 (d, 2H), and 8.78 (br, 1H). 13 C{ 1 H} NMR (125 MHz, C₆D₆): δ 121.44, 125.93 (q), 129.19 (d), 130.09, 134.59 (d), 135.12 (d), 141.78, and 207.84 (d). 31 P{ 1 H} NMR (202 MHz, CDCl₃): δ 21.63. Anal Calcd for C₂₀H₁₅F₃NPS: C, 61.69; H, 3.88; and N, 3.60. Found: C, 61.70; H, 4.10; and N, 3.56. MS (ASAP) m/z calcd for [C₂₀H₁₅F₃NPS + H⁺]: 390.07. Found: 390.07.

Synthesis of N,N'-Disubstituted Thioureas (1a–d). N,N'-Disubstituted thioureas are synthesized following the procedure reported by Hendricks et al.⁸¹

Synthesis of N,N',N'-Trisubstituted Thioureas (2a–g). N,N',N'-Trisubstituted thioureas (2a–e, 2g) are synthesized following a report by Hendricks et al., ⁸¹ and precursor 2f is synthesized following a report by Hamachi et al. ⁸² Compounds 2a and 2e–g are not reported in the literature, and their synthesis and characterization are detailed below. NMR spectra for all new compounds are included in Appendix II.

N-n-Butyl, N',N'-n-Dibutyl Thiourea (2a). Di-*n*-butylamine (2.58 g, 20 mmol) and *n*-butyl isothiocyanate (2.30 g, 20 mmol) are combined in toluene (20 mL) and stirred for >30 min are room temperature. Volatiles are removed *in vacuo* resulting in a viscous, pale yellow oil. Yield is 4.5 g (92%). ¹H NMR (500 MHz, CDCl₃): δ 0.93 (t, 9H), 1.34 (m, 6H), 1.59 (m, 6H), 3.54 (t, 4H), 3.62 (td, 2H), and 5.25 (br, 1H). ¹³C{¹H} NMR (125 MHz, CDCl₃): δ 13.90, 20.26, 29.63, 31.53, 45.93, 50.94, and 180.67. Anal. Calcd for C₁₃H₂₈N₂S: C, 63.88; H, 11.55; and N, 11.46. Found: C, 63.90; H, 11.80; and N, 11.49. MS (ASAP) m/z: calcd for [C₁₃H₂₈N₂S + H⁺]: 245.21. Found: 245.21.

N-Dodecyl, N'-Pyrrolidine Thiourea (**2e**). The crude material (1.1 g) was recrystallized from ethanol to yield 1.0 g (88%) of **2e** as white crystals (3.95 mmol scale). 1 H NMR (500 MHz, CDCl₃): δ 0.88 (t, 3H), 1.25 (m, 18H), 1.60 (quint, 2H), 3.94 (br, 4H), 3.58 (br, 4H), 3.63 (td, 2H), and 5.12 (br, 1H). 13 C{ 1 H} NMR (125 MHz, CDCl₃): δ 14.27, 22.84, 27.11, 29.49, 29.52, 29.71, 29.73, 29.77, 29.80, 32.06, 45.80, and 178.77. Anal. Calcd for C₁₇H₃₄N₂S: C, 68.40; H, 11.48; and N, 9.38. Found: C, 68.37; H, 11.23; and N, 9.33. MS (ASAP) m/z calcd for [C₁₇H₃₄N₂S + H⁺]: 299.25. Found: 299.25.

N-4-Methoxy-Phenyl, N',N'-n-Dibutyl Thiourea (2f). The crude material was collected as a light yellow powder, recrystallized from toluene/hexanes and dried under vacuum for >6 h to yield 1.8 g

(86%) of **2f** was white crystals (7.6 mmol scale). 1 H NMR (500 MHz, CDCl₃): δ 0.97 (t, 6H), 1.39 (sextet, 4H), 1.71 (m, 4H), 3.67 (t, 4H), 3.81 (s, 3H), 6.87 (br, 1H), 6.88 (d, 2H), and 7.21 (s, 2H). 13 C{ 1 H} NMR (125 MHz, CDCl₃): δ 13.90, 20.29, 29.62, 51.50, 55.44, 114.01, 128.00, 132.74, 157.83, and 181.72. Anal Calcd for C₁₆H₂₆N₂OS: C, 65.26; H, 8.90; and N, 9.51. Found: C, 65.38; H, 8.87; and N, 9.53. MS (ASAP) m/z calcd for [C₁₆H₂₆N₂OS + H⁺]: 295.18. Found: 295.18.

N-4-Trifluoromethyl-Phenyl, N',N'-n-Dibutyl Thiourea (**2g**). The crude material (1.5 g) was recrystallized from ethanol and dried under vacuum for >6 h to yield 1.3 g (78%) of **2g** as white crystals (run on 5 mmol scale). ¹H NMR (500 MHz, CDCl₃): δ 0.98 (t, 6H), 1.40 (sextet, 4H), 1.72 (m, 4H), 3.69 (t, 4H), 7.00 (s, 1H), 7.47 (d, 2H), and 7.58 (d, 2H). ¹³C{ ¹H } NMR (125 MHz, CDCl₃): δ 13.99, 20.39, 29.70, 51.78, 124.43, 125.99 (q), 143.09, and 180.87. Anal Calcd for C₁₆H₂₃F₃N₂S: C, 57.81; H, 6.97; and N, 8.43. Found: C, 57.96; H, 6.89; and N, 8.43. MS (ASAP) m/z calcd for [C₁₆H₂₃F₃N₂S + H⁺]: 333.16. Found: 333.16.

Synthesis of ZnS Nanocrystals from Zinc Oleate. In an inert atmosphere glovebox, zinc oleate (0.226 g, 0.36 mmol, 1.5 equiv) and 1-octadecene (8.99 g, 11.4 mL) are added to a 50 mL three-neck round-bottom flask equipped with a stir bar and sealed with an air-free vacuum adapter and two rubber septa. The desired thiourea (e.g., Nhexyl-N'-dodecyl thiourea (0.079 g, 0.24 mmol)) and tetraglyme (0.61 g, 0.6 mL) are added to a 4 mL vial equipped with a stir bar and sealed with a rubber septum. After transferring to a Schlenk line, the vessels are attached to an argon inlet. The three-neck round bottom flask is heated rapidly to the desired temperature (e.g., 240 °C), and the 4 mL vial is heated to 80 °C. After the temperature stabilizes, the thiourea solution is swiftly injected into the round-bottom flask containing the clear, colorless zinc oleate solution. The reaction is run for the optimum reaction time according to the data shown in Tables S1 and S2 (e.g., 5 min) before being removed from the heating mantle and allowed to cool to room temperature. Upon a white suspension forming, the reaction is split into two 50 mL centrifuge tubes. Acetone (30 mL) is added to precipitate nanocrystals in each tube, appearing cloudy white and opaque. After centrifugation (8000 rpm, 7 min), the supernatant is decanted, and hexanes (2 mL per tube) are added to white pellets. The resulting suspension is filtered using a 0.2 μ M pore size syringe filter into a 50 mL centrifuge tube. Acetone is added (30 mL) forming an opaque white suspension. After centrifugation (8000 rpm, 7 min), the supernatant is discarded and the white solid redispersed in hexanes (2 mL). The cycle of precipitation from hexanes with acetone was performed four times in total. Note: this procedure can be scaled up 3× without a noticeable change in product quality. No attempt was made to scale further.

Synthesis of ZnS Nanocrystals from Zinc Tetradecanoate. Reactions using zinc tetradecanoate instead of zinc oleate were carried out with the following modifications: (1) hexadecane is used in place of 1-octadecene and (2) upon cooling to 100 °C at the end of the reaction, oleic acid (2.20 mmol, 0.68 mL) is injected.

Synthesis of ZnS Nanocrystals from Zinc 2-Hexyldecanoate. Reactions using zinc 2-hexyldecanoate instead of zinc oleate were carried out with the following modifications: (1) upon cooling to 100 $^{\circ}$ C at end of reaction, no oleic acid is added and (2) 1-octadecene and hexadecane can be used interchangeably. Precipitation can occur during reactions where large nanocrystals are being grown (estimated d>6 nm) and the addition of oleic acid will help solubilize. Additionally, during the isolation steps, nanocrystals can irreversibly precipitate due to stripping of the ligands. The addition of octylamine will help resolubilize.

Synthesis of ZnS with Added Zinc Acetate. ZnS was synthesized using the method outlined for synthesis from zinc oleate, with the addition of zinc acetate, maintaining the initial Zn/S ratio of 1.5:1. For example, the three-neck round-bottom flask preparation for 10% acetate: zinc oleate (0.204 g, 0.32 mmol, 1.35 equiv), zinc acetate (0.0066 g, 0.04 mmol, 0.15 equiv), and 1-octadecene (8.99 g, 11.4 mL) are loaded into a 50 mL three-neck round-bottom flask in an inert atmosphere.

UV–Visible Absorption Spectroscopy of Aliquots. Aliquots (50 μ L) from the reaction are diluted with hexanes (3 mL), and the UV–visible absorption is measured (λ = 200–400 nm). For reactions using a thiourea containing an aryl group, aliquots are washed once before obtaining UV–visible absorption. For aliquots used for STEM imaging, aliquots are washed twice (without syringe filter step) and then redistributed in hexanes. Further details are provided in the Supporting Information.

X-ray Total Scattering Experiments. ZnS nanocrystals are synthesized and purified on 35 mL scale and then dried under vacuum for 6 h. For the smallest diameter dots, a sticky white paste forms; for the larger dots, a white powder was formed. Samples are loaded into polyimide tubing (OD: 0.0750", ID: 0.0710") in air and sealed with modeling clay. X-ray total scattering measurements are performed at the National Synchrotron Light Source II (XPD, 28-ID2), Brookhaven National Laboratory. Diffraction patterns for the ZnS size series are collected at room temperature in a transmission geometry with an X-ray energy of 66.874 keV ($\lambda = 0.1854 \text{ Å}$) using a large area 2D PerkinElmer detector. The detector is mounted with a sample-to-detector distance of 204.64 mm. The experimental geometry, 2θ range, and detector misorientations are calibrated by measuring a crystalline nickel powder directly prior to the ZnS nanocrystals, with the experimental geometry parameters refined using the Fit2D program. 105 Standardized corrections are then made to the data to obtain the total scattering structure functions, 106,107 as detailed in the Supporting Information.

Pair Distribution Function Analysis Modeling. Optimized parameter values for calculating the model reduced pair distribution function G(r) are obtained using least-squares refinement in PDFgui¹⁰⁸ using an established method to account for the finite size effects and mixed-phase zincblende/wurtzite structure of nanoparticles. Further details are included in the Supporting Information.

Sample Preparation for HAADF-STEM. Nanocrystals are isolated by washing at least three times, as per the instructions listed above, and redistributed in hexanes. For STEM on reaction aliquots, aliquots are washed twice and redistributed in hexanes. Samples are diluted and UV–vis spectra are obtained. Dilution is adjusted such that the absorbance intensity of the peak is the following: \leq 0.6 for nanocrystals with $\lambda_{\max} = 270-280$ nm, \leq 0.2 for nanocrystals with $\lambda_{\max} = 280-290$ nm, and \leq 0.1 for nanocrystals with $\lambda_{\max} = 290+$ nm. TEM grids are held at the edge by tweezers and one drop of the nanocrystal solution is added and the solvent allowed to evaporate. TEM grids are dried under vacuum for >2 h before imaging.

Size Determination of ZnS Using HAADF-STEM. To minimize the error between samples, a consistent magnification (630k×) was used to acquire the micrographs. HAADF-STEM images were imported into ImageJ as a tif file, and the scale bar was set using the scale from the micrograph. For samples containing uniform and spherical ZnS, nanocrystals were measured individually using the circle tool. An oval or polygon selection was occasionally used if deemed more appropriate. The measured areas were then converted to the radius that corresponds to a circle with the same area. Highly anisotropic nanocrystals were not analyzed in this manner and were not included in the sizing curve fit. Further specific details and discussion of errors are included in the Supporting Information, Section III.

Postsynthetic Ligand Exchange. Following the procedure from Dhaene et al., 83 native oleate ligands are exchanged for (6-[2-[2-(2-methoxy-ethoxy)-ethoxy]-ethoxy]hexyl) phosphonate ligands. Briefly, nanocrystals are isolated by washing as per the instructions above. The sample is dried under vacuum and taken up in chloroform- d_3 (\sim 0.5 mL). The concentration of oleate is estimated using $^1\mathrm{H}$ NMR and the ERETIC method. 111 Approximately 2 equiv of (6-[2-[2-(2-methoxy-ethoxy)-ethoxy]-ethoxy]hexyl) phosphonic acid per oleate is added, and the solution is left to stir for 10 min. NCs are precipitated with hexanes. After centrifugation, the supernatant is discarded and NCs are dispersed in minimal chloroform. This wash is repeated twice

ASSOCIATED CONTENT

Supporting Information

The Supporting Information is available free of charge at https://pubs.acs.org/doi/10.1021/acs.chemmater.1c03432.

Discussion of aliquot methods, ZnS shape anisotropy, sizing methods, and sizing curve determination; Figures S1–S45; Tables S1–S12; UV absorbance spectra, electron micrographs, and size distribution histograms for nanocrystals used in sizing curve determination; and 1 H, 13 C, 19 F, and 31 P NMR spectra for newly synthesized compounds (PDF)

AUTHOR INFORMATION

Corresponding Author

Jonathan S. Owen — Department of Chemistry, Columbia University, New York, New York 10027, United States; orcid.org/0000-0001-5502-3267; Email: jso2115@columbia.edu

Authors

Ellie Bennett — Department of Chemistry, Columbia University, New York, New York 10027, United States; orcid.org/0000-0003-2714-2773

Matthew W. Greenberg – Department of Chemistry, Columbia University, New York, New York 10027, United States; © orcid.org/0000-0002-5081-3099

Abraham J. Jordan – Department of Chemistry, Columbia University, New York, New York 10027, United States; orcid.org/0000-0002-4343-5675

Leslie S. Hamachi — Department of Chemistry, Columbia University, New York, New York 10027, United States; Department of Chemistry and Biochemistry, California Polytechnic State University, San Luis Obispo, California 93407, United States; orcid.org/0000-0001-6299-8695

Soham Banerjee — Department of Applied Physics and Applied Mathematics, Columbia University, New York, New York 10027, United States; orcid.org/0000-0001-9271-493X

Simon J. L. Billinge — Department of Applied Physics and Applied Mathematics, Columbia University, New York, New York 10027, United States; Condensed Matter Physics and Materials Science Department, Brookhaven National Laboratory, Upton, New York 11973, United States; orcid.org/0000-0002-9734-4998

Complete contact information is available at: https://pubs.acs.org/10.1021/acs.chemmater.1c03432

Notes

The authors declare no competing financial interest.

ACKNOWLEDGMENTS

Mechanistic and size control studies were supported by the National Science Foundation under Award Number 2004008. ZnS shelling work was supported by the National Science Foundation under Award Number 1827726. Work in the Billinge group was supported by U.S. Department of Energy, Office of Science, Office of Basic Energy Sciences (DOE-BES) under Contract No. DESC00112704. S.B. acknowledges support from the National Defense Science and Engineering Graduate Fellowship (DOD-NDSEG) program. X-ray PDF measurements were conducted on beamline 28-ID-2 of the National Synchrotron Light Source II, a U.S. Department of

Energy (DOE) Office of Science User Facility operated for the DOE Office of Science by Brookhaven National Laboratory under Contract No. DE-SC0012704. The authors would like to acknowledge Amirali Zangiabadi for helpful electron microscopy discussions and Columbia University's Nanoscience Initiative for use of its shared facilities.

REFERENCES

- (1) Choi, M. K.; Yang, J.; Hyeon, T.; Kim, D.-H. Flexible quantum dot light-emitting diodes for next-generation displays. *npj Flexible Electron.* **2018**, *2*, No. 10.
- (2) Jiang, Y.; Cho, S.-Y.; Shim, M. Light-emitting diodes of colloidal quantum dots and nanorod heterostructures for future emissive displays. *J. Mater. Chem. C* **2018**, *6*, 2618–2634.
- (3) Michalet, X.; Pinaud, F. F.; Bentolila, L. A.; Tsay, J. M.; Doose, S.; Li, J. J.; Sundaresan, G.; Wu, A. M.; Gambhir, S. S.; Weiss, S. Quantum Dots for Live Cells, in Vivo Imaging, and Diagnostics. *Science* **2005**, *307*, 538–544.
- (4) Hernandez-Calderon, I. Optical Properties and Electronic Structure of Wide Band Gap II–VI Semiconductors. In *II–VI Semiconductor Materials and Their Applications*; Routledge, 2018; pp 113–170.
- (5) Reiss, P.; Protière, M.; Li, L. Core/shell semiconductor nanocrystals. *Small* **2009**, *5*, 154–168.
- (6) Talapin, D. V.; Mekis, I.; Götzinger, S.; Kornowski, A.; Benson, O.; Weller, H. CdSe/CdS/ZnS and CdSe/ZnSe/ZnS Core-Shell-Shell Nanocrystals. *J. Phys. Chem. B* **2004**, *108*, 18826–18831.
- (7) Zhang, W.; Li, Y.; Zhang, H.; Zhou, X.; Zhong, X. Facile synthesis of highly luminescent Mn-doped ZnS nanocrystals. *Inorg. Chem.* **2011**, *50*, 10432–10438.
- (8) Buonsanti, R.; Milliron, D. J. Chemistry of Doped Colloidal Nanocrystals. *Chem. Mater.* **2013**, *25*, 1305–1317.
- (9) Norris, D. J.; Efros, A. L.; Erwin, S. C. Doped Nanocrystals. Science 2008, 319, 1776.
- (10) Wu, P.; Yan, X.-P. Doped quantum dots for chemo/biosensing and bioimaging. *Chem. Soc. Rev.* **2013**, *42*, 5489–5521.
- (11) Kim, S.; Kim, J.-A.; Kim, T.; Chung, H.; Park, S.; Choi, S.-M.; Kim, H.-M.; Chung, D.-Y.; Jang, E. Efficient Blue-Light-Emitting Cd-Free Colloidal Quantum Well and Its Application in Electroluminescent Devices. *Chem. Mater.* **2020**, *32*, 5200–5207.
- (12) Jeong, B. G.; Park, Y.-S.; Chang, J. H.; Cho, I.; Kim, J. K.; Kim, H.; Char, K.; Cho, J.; Klimov, V. I.; Park, P.; Lee, D. C.; Bae, W. K. Colloidal Spherical Quantum Wells with Near-Unity Photoluminescence Quantum Yield and Suppressed Blinking. *ACS Nano* **2016**, *10*, 9297–9305.
- (13) Boldt, K.; Kirkwood, N.; Beane, G. A.; Mulvaney, P. Synthesis of Highly Luminescent and Photo-Stable, Graded Shell CdSe/CdxZn1-xS Nanoparticles by In Situ Alloying. *Chem. Mater.* **2013**, 25, 4731–4738.
- (14) Manna, L.; Scher, E. C.; Li, L.-S.; Alivisatos, A. P. Epitaxial Growth and Photochemical Annealing of Graded CdS/ZnS Shells on Colloidal CdSe Nanorods. *J. Am. Chem. Soc.* **2002**, *124*, 7136–7145.
- (15) Protière, M.; Reiss, P. Facile synthesis of monodisperse ZnS capped CdS nanocrystals exhibiting efficient blue emission. *Nanoscale Res. Lett.* **2006**, *1*, No. 62.
- (16) Li, J. J.; Wang, Y. A.; Guo, W.; Keay, J. C.; Mishima, T. D.; Johnson, M. B.; Peng, X. Large-Scale Synthesis of Nearly Monodisperse CdSe/CdS Core/Shell Nanocrystals Using Air-Stable Reagents via Successive Ion Layer Adsorption and Reaction. *J. Am. Chem. Soc.* 2003, 125, 12567–12575.
- (17) Xie, R.; Kolb, U.; Li, J.; Basché, T.; Mews, A. Synthesis and Characterization of Highly Luminescent CdSe-Core CdS/Zn0.5Cd0.5S/ZnS Multishell Nanocrystals. *J. Am. Chem. Soc.* **2005**, 127, 7480-7488.
- (18) Chen, Y.; Vela, J.; Htoon, H.; Casson, J. L.; Werder, D. J.; Bussian, D. A.; Klimov, V. I.; Hollingsworth, J. A. "Giant" Multishell CdSe Nanocrystal Quantum Dots with Suppressed Blinking. *J. Am. Chem. Soc.* **2008**, *130*, 5026–5027.

- (19) van Embden, J.; Jasieniak, J.; Mulvaney, P. Mapping the Optical Properties of CdSe/CdS Heterostructure Nanocrystals: The Effects of Core Size and Shell Thickness. *J. Am. Chem. Soc.* **2009**, *131*, 14299–14309.
- (20) Greytak, A. B.; Allen, P. M.; Liu, W.; Zhao, J.; Young, E. R.; Popović, Z.; Walker, B. J.; Nocera, D. G.; Bawendi, M. G. Alternating layer addition approach to CdSe/CdS core/shell quantum dots with near-unity quantum yield and high on-time fractions. *Chem. Sci.* **2012**, 3, 2028–2034.
- (21) Ithurria, S.; Talapin, D. V. Colloidal Atomic Layer Deposition (c-ALD) using Self-Limiting Reactions at Nanocrystal Surface Coupled to Phase Transfer between Polar and Nonpolar Media. *J. Am. Chem. Soc.* **2012**, *134*, 18585–18590.
- (22) Polovitsyn, A.; Dang, Z.; Movilla, J. L.; Martín-García, B.; Khan, A. H.; Bertrand, G. H. V.; Brescia, R.; Moreels, I. Synthesis of Air-Stable CdSe/ZnS Core—Shell Nanoplatelets with Tunable Emission Wavelength. *Chem. Mater.* **2017**, *29*, 5671–5680.
- (23) Liu, S.; Yu, Q.; Zhang, C.; Zhang, M.; Rowell, N.; Fan, H.; Huang, W.; Yu, K.; Liang, B. Transformation of ZnS Precursor Compounds to Magic-Size Clusters Exhibiting Optical Absorption Peaking at 269 nm. *J. Phys. Chem. Lett.* **2020**, *11*, 75–82.
- (24) Munro, A. M. Synthetic approaches for growing zinc sulfide and zinc selenide colloidal nanocrystals. *J. Vac. Sci. Technol. A* **2020**, 38, No. 020805.
- (25) Li, H.; Shih, W. Y.; Shih, W.-H. Stable aqueous ZnS quantum dots obtained using (3-mercaptopropyl)trimethoxysilane as a capping molecule. *Nanotechnology* **2007**, *18*, No. 495605.
- (26) Li, H.; Shih, W. Y.; Shih, W.-H. Non-heavy-metal ZnS quantum dots with bright blue photoluminescence by a one-step aqueous synthesis. *Nanotechnology* **2007**, *18*, No. 205604.
- (27) Rossetti, R.; Hull, R.; Gibson, J. M.; Brus, L. E. Excited electronic states and optical spectra of ZnS and CdS crystallites in the ≈15 to 50 Å size range: Evolution from molecular to bulk semiconducting properties. *J. Chem. Phys.* 1985, 82, 552–559.
- (28) Bochev, B.; Yordanov, G. Room temperature synthesis of thioglycolate-coated zinc sulfide (ZnS) nanoparticles in aqueous medium and their physicochemical characterization. *Colloids Surf., A* **2014**, *441*, 84–90.
- (29) Juine, R. N.; Das, A.; Amirthapandian, S. Concentration controlled QDs ZnS synthesis without capping agent and its optical properties. *Mater. Lett.* **2014**, *128*, 160–162.
- (30) Baruah, J. M.; Kalita, S.; Narayan, J. Green chemistry synthesis of biocompatible ZnS quantum dots (QDs): their application as potential thin films and antibacterial agent. *Int. Nano Lett.* **2019**, *9*, 149–159.
- (31) He, J.; Ji, W.; Mi, J.; Zheng, Y.; Ying, J. Y. Three-photon absorption in water-soluble ZnS nanocrystals. *Appl. Phys. Lett.* **2006**, 88, No. 181114.
- (32) Chandrakar, R. K.; Baghel, R. N.; Chandra, V. K.; Chandra, B. P. Synthesis, characterization and photoluminescence studies of undoped ZnS nanoparticles. *Superlattices Microstruct.* **2015**, *84*, 132–143
- (33) Joo, J.; Na, H. B.; Yu, T.; Yu, J. H.; Kim, Y. W.; Wu, F.; Zhang, J. Z.; Hyeon, T. Generalized and Facile Synthesis of Semiconducting Metal Sulfide Nanocrystals. *J. Am. Chem. Soc.* **2003**, *125*, 11100–11105.
- (34) Zhai, X.; Zhang, X.; Chen, S.; Yang, W.; Gong, Z. Oleylamine as solvent and stabilizer to synthesize shape-controlled ZnS nanocrystals with good optical properties. *Colloids Surf., A* **2012**, 409, 126–129.
- (35) Li, L. S.; Pradhan, N.; Wang, Y.; Peng, X. High Quality ZnSe and ZnS Nanocrystals Formed by Activating Zinc Carboxylate Precursors. *Nano Lett.* **2004**, *4*, 2261–2264.
- (36) Xiao, N.; Dai, Q.; Wang, Y.; Ning, J.; Liu, B.; Zou, G.; Zou, B. ZnS nanocrystals and nanoflowers synthesized by a green chemistry approach: Rare excitonic photoluminescence achieved by the tunable molar ratio of precursors. *J. Hazard. Mater.* **2012**, *211-212*, 62–67.

- (37) Shahid, R.; Toprak, M. S.; Soliman, H. M. A.; Muhammed, M. Low temperature synthesis of cubic phase zinc sulfide quantum dots. *Cent. Eur. J. Chem.* **2012**, *10*, 54–58.
- (38) Yu, J. H.; Joo, J.; Park, H. M.; Baik, S.-I.; Kim, Y. W.; Kim, S. C.; Hyeon, T. Synthesis of Quantum-Sized Cubic ZnS Nanorods by the Oriented Attachment Mechanism. *J. Am. Chem. Soc.* **2005**, *127*, 5662–5670.
- (39) Li, Y.; Li, X.; Yang, C.; Li, Y. Ligand-Controlling Synthesis and Ordered Assembly of ZnS Nanorods and Nanodots. *J. Phys. Chem. B* **2004**, *108*, 16002–16011.
- (40) Xia, Y.; Zhai, G.; Zheng, Z.; Lian, L.; Liu, H.; Zhang, D.; Gao, J.; Zhai, T.; Zhang, J. Solution-processed solar-blind deep ultraviolet photodetectors based on strongly quantum confined ZnS quantum dots. J. Mater. Chem. C 2018, 6, 11266–11271.
- (41) Kan, H.; Zheng, W.; Lin, R.; Li, M.; Fu, C.; Sun, H.; Dong, M.; Xu, C.; Luo, J.; Fu, Y.; Huang, F. Ultrafast Photovoltaic-Type Deep Ultraviolet Photodetectors Using Hybrid Zero-/Two-Dimensional Heterojunctions. ACS Appl. Mater. Interfaces 2019, 11, 8412–8418.
- (42) Lu, S. H.; Chen, T. F.; Wang, A. J.; Wu, Z. L.; Wang, Y. S. Lattice and optical property evolution of ultra-small ZnS quantum dots grown from a single-source precursor. *Appl. Surf. Sci.* **2014**, 299, 116–122.
- (43) Zhang, Y.; Xu, H.; Wang, Q. Ultrathin single crystal ZnS nanowires. Chem. Commun. 2010, 46, 8941–8943.
- (44) Hoa, T. T. Q.; Vu, L. V.; Canh, T. D.; Long, N. N. Preparation of ZnS nanoparticles by hydrothermal method. *J. Phys.: Conf. Ser.* **2009**, *187*, No. 012081.
- (45) Dawood, F.; Schaak, R. E. ZnO-Templated Synthesis of Wurtzite-Type ZnS and ZnSe Nanoparticles. *J. Am. Chem. Soc.* **2009**, 131, 424–425.
- (46) Dengo, N.; Vittadini, A.; Natile, M. M.; Gross, S. In-Depth Study of ZnS Nanoparticle Surface Properties with a Combined Experimental and Theoretical Approach. J. Phys. Chem. C 2020, 124, 7777–7789
- (47) Dumbrava, A.; Badea, C.; Prodan, G.; Popovici, I.; Ciupina, V. Zinc sulfide fine particles obtained at low temperature. *Chalcogenide Lett.* **2009**, *6*, 437–443.
- (48) Buffard, A.; Nadal, B.; Heuclin, H.; Patriarche, G.; Dubertret, B. ZnS anisotropic nanocrystals using a one-pot low temperature synthesis. *New J. Chem.* **2015**, *39*, 90–93.
- (49) Dai, L.; Lesyuk, R.; Karpulevich, A.; Torche, A.; Bester, G.; Klinke, C. From Wurtzite Nanoplatelets to Zinc Blende Nanorods: Simultaneous Control of Shape and Phase in Ultrathin ZnS Nanocrystals. *J. Phys. Chem. Lett.* **2019**, *10*, 3828–3835.
- (50) Wang, Y.; Zhou, Y.; Zhang, Y.; Buhro, W. E. Magic-Size II–VI Nanoclusters as Synthons for Flat Colloidal Nanocrystals. *Inorg. Chem.* **2015**, *54*, 1165–1177.
- (51) Deng, Z.; Yan, H.; Liu, Y. Controlled Colloidal Growth of Ultrathin Single-Crystal ZnS Nanowires with a Magic-Size Diameter. *Angew. Chem., Int. Ed.* **2010**, 49, 8695–8698.
- (52) Xing, G.; Liu, X.; Hao, S.; Li, X.; Fan, L.; Li, Y. Diameter- and Length-controlled Synthesis of Ultrathin ZnS Nanowires and Their Size-Dependent UV Absorption Properties, Photocatalytical Activities and Band-Edge Energy Levels. *Nanomaterials* **2019**, *9*, No. 220.
- (53) Ji, B.; Koley, S.; Slobodkin, I.; Remennik, S.; Banin, U. ZnSe/ZnS Core/Shell Quantum Dots with Superior Optical Properties through Thermodynamic Shell Growth. *Nano Lett.* **2020**, *20*, 2387–2395.
- (54) Ji, B.; Panfil, Y. E.; Waiskopf, N.; Remennik, S.; Popov, I.; Banin, U. Strain-controlled shell morphology on quantum rods. *Nat. Commun.* **2019**, *10*, No. 2.
- (55) Jasieniak, J.; Smith, L.; van Embden, J.; Mulvaney, P.; Califano, M. Re-examination of the Size-Dependent Absorption Properties of CdSe Quantum Dots. *J. Phys. Chem. C* **2009**, *113*, 19468–19474.
- (56) Yu, W. W.; Qu, L.; Guo, W.; Peng, X. Experimental Determination of the Extinction Coefficient of CdTe, CdSe and CdS Nanocrystals. *Chem. Mater.* **2004**, *16*, 560.
- (57) Moreels, I.; Lambert, K.; De Muynck, D.; Vanhaecke, F.; Poelman, D.; Martins, J. C.; Allan, G.; Hens, Z. Composition and

- Size-Dependent Extinction Coefficient of Colloidal PbSe Quantum Dots. *Chem. Mater.* **2007**, *19*, 6101–6106.
- (58) Moreels, I.; Lambert, K.; Smeets, D.; De Muynck, D.; Nollet, T.; Martins, J. C.; Vanhaecke, F.; Vantomme, A.; Delerue, C.; Allan, G.; Hens, Z. Size-Dependent Optical Properties of Colloidal PbS Quantum Dots. *ACS Nano* **2009**, *3*, 3023–3030.
- (59) Nakaoka, Y.; Nosaka, Y. Electron Spin Resonance Study of Radicals Produced by Photoirradiation on Quantized and Bulk ZnS Particles. *Langmuir* **1997**, *13*, 708–713.
- (60) Barman, B.; Chandra Sarma, K. Low temperature chemical synthesis of ZnS, Mn doped ZnS nanosized particles: Their structural, morphological and photophysical properties. *Solid State Sci.* **2020**, *109*, No. 106404.
- (61) Vogel, W.; Borse, P. H.; Deshmukh, N.; Kulkarni, S. K. Structure and Stability of Monodisperse 1.4-nm ZnS Particles Stabilized by Mercaptoethanol. *Langmuir* **2000**, *16*, 2032–2037.
- (62) Wang, Y. H.; Chen, Z.; Zhou, X. Q. Synthesis and Photoluminescence of ZnS Quantum Dots. *J. Nanosci. Nanotechnol.* **2008**, *8*, 1312–1315.
- (63) Kho, R.; Torres-Martínez, C. L.; Mehra, R. K. A Simple Colloidal Synthesis for Gram-Quantity Production of Water-Soluble ZnS Nanocrystal Powders. *J. Colloid Interface Sci.* **2000**, 227, 561–566.
- (64) Mahamuni, S.; Khosravi, A. A.; Kundu, M.; Kshirsagar, A.; Bedekar, A.; Avasare, D. B.; Singh, P.; Kulkarni, S. K. Thiophenol-capped ZnS quantum dots. *J. Appl. Phys.* **1993**, *73*, 5237–5240.
- (65) Nanda, J.; Sapra, S.; Sarma, D. D.; Chandrasekharan, N.; Hodes, G. Size-Selected Zinc Sulfide Nanocrystallites: Synthesis, Structure, and Optical Studies. *Chem. Mater.* **2000**, *12*, 1018–1024.
- (66) Zhao, Y.; Zhang, Y.; Zhu, H.; Hadjipanayis, G. C.; Xiao, J. Q. Low-temperature synthesis of hexagonal (wurtzite) ZnS nanocrystals. *J. Am. Chem. Soc.* **2004**, *126*, 6874–6875.
- (67) Kortan, A. R.; Hull, R.; Opila, R. L.; Bawendi, M. G.; Steigerwald, M. L.; Carroll, P. J.; Brus, L. E. Nucleation and Growth of CdSe on ZnS Quantum Crystallite Seeds, and Vice Versa, in Inverse Micelle Media. J. Am. Chem. Soc. 1990, 112, 1327–1332.
- (68) Kuzuya, T.; Tai, Y.; Yamamuro, S.; Sumiyama, K. Size-focusing of ZnS nanocrystals observed by MALDI-TOF mass spectroscopy. *Chem. Phys. Lett.* **2005**, *407*, 460–463.
- (69) Khitrov, G. A.; Strouse, G. F. ZnS Nanomaterial Characterization by MALDI-TOF Mass Spectrometry. *J. Am. Chem. Soc.* **2003**, 125, 10465–10469.
- (70) Brus, L. E. Electron–electron and electron-hole interactions in small semiconductor crystallites: The size dependence of the lowest excited electronic state. *J. Chem. Phys.* **1984**, *80*, 4403–4409.
- (71) Brus, L. Electronic wave functions in semiconductor clusters: experiment and theory. *J. Phys. Chem. A* **1986**, *90*, 2555–2560.
- (72) Maes, J.; Castro, N.; De Nolf, K.; Walravens, W.; Abécassis, B.; Hens, Z. Size and Concentration Determination of Colloidal Nanocrystals by Small-Angle X-ray Scattering. *Chem. Mater.* **2018**, 30, 3952–3962.
- (73) Masadeh, A. S. Total scattering atomic pair distribution function: new methodology for nanostructure determination. *J. Exp. Nanosci.* **2016**, *11*, 951–974.
- (74) Masadeh, A. S.; Božin, E. S.; Farrow, C. L.; Paglia, G.; Juhas, P.; Billinge, S. J. L.; Karkamkar, A.; Kanatzidis, M. G. Quantitative size-dependent structure and strain determination of CdSe nanoparticles using atomic pair distribution function analysis. *Phys. Rev. B* **2007**, *76*, No. 115413.
- (75) Gilbert, B. Finite size effects on the real-space pair distribution function of nanoparticles. *J. Appl. Crystallogr.* **2008**, *41*, 554–562.
- (76) Billinge, S. J. L.; Kanatzidis, M. G. Beyond crystallography: the study of disorder, nanocrystallinity and crystallographically challenged materials with pair distribution functions. *Chem. Commun.* **2004**, 749–760.
- (77) Yang, X.; Masadeh, A. S.; McBride, J. R.; Božin, E. S.; Rosenthal, S. J.; Billinge, S. J. Confirmation of disordered structure of ultrasmall CdSe nanoparticles from X-ray atomic pair distribution function analysis. *Phys. Chem. Chem. Phys.* **2013**, *15*, 8480–8486.

- (78) Neder, R. B.; Korsunskiy, V. I.; Chory, C.; Müller, G.; Hofmann, A.; Dembski, S.; Graf, C.; Rühl, E. Structural characterization of II-VI semiconductor nanoparticles. *Phys. Status Solidi C* **2007**, *4*, 3221–3233.
- (79) Gilbert, B.; Huang, F.; Zhang, H.; Waychunas, G. A.; Banfield, J. F. Nanoparticles: strained and stiff. *Science* **2004**, *305*, 651–654.
- (80) Gilbert, B.; Huang, F.; Lin, Z.; Goodell, C.; Zhang, H.; Banfield, J. F. Surface Chemistry Controls Crystallinity of ZnS Nanoparticles. *Nano Lett.* **2006**, *6*, 605–610.
- (81) Hendricks, M. P.; Campos, M. P.; Cleveland, G. T.; Jen-La Plante, I.; Owen, J. S. A tunable library of substituted thiourea precursors to metal sulfide nanocrystals. *Science* **2015**, 348, 1226–1230.
- (82) Hamachi, L. S.; Jen-La Plante, I.; Coryell, A. C.; De Roo, J.; Owen, J. S. Kinetic Control over CdS Nanocrystal Nucleation Using a Library of Thiocarbonates, Thiocarbamates, and Thioureas. *Chem. Mater.* **2017**, 29, 8711–8719.
- (83) Dhaene, E.; Billet, J.; Bennett, E.; Van Driessche, I.; De Roo, J. The Trouble with ODE: Polymerization during Nanocrystal Synthesis. *Nano Lett.* **2019**, *19*, 7411–7417.
- (84) García-Rodríguez, R.; Hendricks, M. P.; Cossairt, B. M.; Liu, H.; Owen, J. S. Conversion Reactions of Cadmium Chalcogenide Nanocrystal Precursors. *Chem. Mater.* **2013**, *25*, 1233–1249.
- (85) Banski, M.; Afzaal, M.; Malik, M. A.; Podhorodecki, A.; Misiewicz, J.; O'Brien, P. Special Role for Zinc Stearate and Octadecene in the Synthesis of Luminescent ZnSe Nanocrystals. *Chem. Mater.* **2015**, 27, 3797–3800.
- (86) Chiu, W. S.; Khiew, P. S.; Isa, D.; Cloke, M.; Radiman, S.; Abd-Shukor, R.; Abdullah, M. H.; Huang, N. M. Synthesis of two-dimensional ZnO nanopellets by pyrolysis of zinc oleate. *Chem. Eng. J.* **2008**, *142*, 337–343.
- (87) Choi, S.-H.; Kim, E.-G.; Park, J.; An, K.; Lee, N.; Kim, S. C.; Hyeon, T. Large-Scale Synthesis of Hexagonal Pyramid-Shaped ZnO Nanocrystals from Thermolysis of Zn-Oleate Complex. *J. Phys. Chem. B* **2005**, *109*, 14792–14794.
- (88) Campos, M. P.; Hendricks, M. P.; Beecher, A. N.; Walravens, W.; Swain, R. A.; Cleveland, G. T.; Hens, Z.; Sfeir, M. Y.; Owen, J. S. A Library of Selenourea Precursors to PbSe Nanocrystals with Size Distributions near the Homogeneous Limit. *J. Am. Chem. Soc.* **2017**, 139, 2296–2305.
- (89) Owen, J. S.; Chan, E. M.; Liu, H.; Alivisatos, A. P. Precursor Conversion Kinetics and the Nucleation of Cadmium Selenide Nanocrystals. *J. Am. Chem. Soc.* **2010**, *132*, 18206–18213.
- (90) Abe, S.; Čapek, R. K.; De Geyter, B.; Hens, Z. Tuning the Postfocused Size of Colloidal Nanocrystals by the Reaction Rate: From Theory to Application. ACS Nano 2012, 6, 42–53.
- (91) Campos, M. P.; De Roo, J.; Greenberg, M. W.; McMurtry, B. M.; Hendricks, M. P.; Bennett, E.; Saenz, N.; Sfeir, M. Y.; Abécassis, B.; Ghose, S.; Owen, J. S. Growth Kinetics Determine the Polydispersity and Size of PbS and PbSe Nanocrystals, 2021 (submitted for publication).
- (92) McMurtry, B. M.; Qian, K.; Teglasi, J. K.; Swarnakar, A. K.; De Roo, J.; Owen, J. S. Continuous Nucleation and Size Dependent Growth Kinetics of Indium Phosphide Nanocrystals. *Chem. Mater.* **2020**, *32*, 4358–4368.
- (93) Liu, S.; Yu, Q.; Zhang, C.; Zhang, M.; Rowell, N.; Fan, H.; Huang, W.; Yu, K.; Liang, B. Transformation of ZnS Precursor Compounds to Magic-Size Clusters Exhibiting Optical Absorption Peaking at 269 nm. J. Phys. Chem. Lett. 2019, 75–82.
- (94) De Nolf, K.; Cosseddu, S. M.; Jasieniak, J. J.; Drijvers, E.; Martins, J. C.; Infante, I.; Hens, Z. Binding and Packing in Two-Component Colloidal Quantum Dot Ligand Shells: Linear versus Branched Carboxylates. J. Am. Chem. Soc. 2017, 139, 3456–3464.
- (95) Yang, Y. A.; Wu, H.; Williams, K. R.; Cao, Y. C. Synthesis of CdSe and CdTe nanocrystals without precursor injection. *Angew. Chem., Int. Ed.* **2005**, 44, 6712–6715.
- (96) Ithurria, S.; Dubertret, B. Quasi 2D Colloidal CdSe Platelets with Thicknesses Controlled at the Atomic Level. *J. Am. Chem. Soc.* **2008**, *130*, 16504–16505.

- (97) Bertrand, G. H. V.; Polovitsyn, A.; Christodoulou, S.; Khan, A. H.; Moreels, I. Shape control of zincblende CdSe nanoplatelets. *Chem. Commun.* **2016**, *52*, 11975–11978.
- (98) Houtepen, A. J.; Koole, R.; Vanmaekelbergh, D.; Meeldijk, J.; Hickey, S. G. The Hidden Role of Acetate in the PbSe Nanocrystal Synthesis. *J. Am. Chem. Soc.* **2006**, *128*, *6792*–*6793*.
- (99) Carbone, L.; Kudera, S.; Carlino, E.; Parak, W. J.; Giannini, C.; Cingolani, R.; Manna, L. Multiple Wurtzite Twinning in CdTe Nanocrystals Induced by Methylphosphonic Acid. *J. Am. Chem. Soc.* **2006**, *128*, 748–755.
- (100) Calcabrini, M.; Van den Eynden, D.; Ribot, S. S.; Pokratath, R.; Llorca, J.; De Roo, J.; Ibáñez, M. Ligand Conversion in Nanocrystal Synthesis: The Oxidation of Alkylamines to Fatty Acids by Nitrate. *JACS Au* **2021**, *1*, 1898–1903.
- (101) Voznyy, O.; Levina, L.; Fan, J. Z.; Askerka, M.; Jain, A.; Choi, M.-J.; Ouellette, O.; Todorović, P.; Sagar, L. K.; Sargent, E. H. Machine Learning Accelerates Discovery of Optimal Colloidal Quantum Dot Synthesis. *ACS Nano* **2019**, *13*, 11122–11128.
- (102) Weidman, M. C.; Beck, M. E.; Hoffman, R. S.; Prins, F.; Tisdale, W. A. Monodisperse, Air-Stable PbS Nanocrystals via Precursor Stoichiometry Control. ACS Nano 2014, 8, 6363–6371.
- (103) Yang, Y. A.; Wu, H.; Williams, K. R.; Cao, Y. C. Synthesis of CdSe and CdTe Nanocrystals without Precursor Injection. *Angew. Chem., Int. Ed.* **2005**, 44, 6712–6715.
- (104) Itazaki, M.; Matsutani, T.; Nochida, T.; Moriuchi, T.; Nakazawa, H. Convenient synthesis of phosphinecarboxamide and phosphinecarbothioamide by hydrophosphination of isocyanates and isothiocyanates. *Chem. Commun.* **2020**, *56*, 443–445.
- (105) Hammersley, A. P. Fit2d v12.012 Reference Manual v6.0. ESRF Internal Report, ESRF98HA01T, 2004.
- (106) Juhás, P.; Ďavis, T.; Farrow, C. L.; Billinge, S. J. L. PDFgetX3: a rapid and highly automatable program for processing powder diffraction data into total scattering pair distribution functions. *J. Appl. Crystallogr.* **2013**, *46*, 560–566.
- (107) Yang, X.; Juhas, P.; Farrow, C. L.; Billinge, S. J. L. xPDFsuite: An End-to-End Software Solution for High Throughput Pair Distribution Function Transformation, Visualization and Analysis, 2015. arXiv:1402.3163. https://arxiv.org/abs/1402.3163.
- (108) Farrow, C.; Juhas, P.; Liu, J.; Bryndin, D.; Božin, E.; Bloch, J.; Proffen, T.; Billinge, S. PDFfit2 and PDFgui: computer programs for studying nanostructure in crystals. *J. Phys.: Condens. Matter* **2007**, *19*, No. 335219.
- (109) Kodama, K.; Iikubo, S.; Taguchi, T.; Shamoto, S. Finite size effects of nanoparticles on the atomic pair distribution functions. *J. Acta Crystallogr., Sect. A* **2006**, *62*, 444–453.
- (110) Pyrz, W. D.; Buttrey, D. J. Particle Size Determination Using TEM: A Discussion of Image Acquisition and Analysis for the Novice Microscopist. *Langmuir* **2008**, *24*, 11350–11360.
- (111) Akoka, S.; Barantin, L.; Trierweiler, M. Concentration Measurement by Proton NMR Using the ERETIC Method. *Anal. Chem.* **1999**, *71*, 2554–2557.